Metals and Materials International
https://doi.org/10.1007/s12540-023-01602-8

Using Solution Heat Treatment and Multi Directional Forging to Improve the Mechanical and Corrosion Properties of an Mg–2Zn–0.2Ag Alloy

Mohammad Asadollahi[1] · Reza Alizadeh[1] · Reza Mahmudi[2] · Sheyda Labbaf[3,4] · Sayed Khatiboleslam Sadrnezhaad[1] · Mehdi Atari[3]

Received: 6 September 2023 / Accepted: 5 December 2023
© The Author(s) under exclusive licence to The Korean Institute of Metals and Materials 2024

Abstract
This study investigated the effects of solution heat treatment and multi-directional forging (MDF) on the microstructure, mechanical, and corrosion properties of an Mg–2Zn–0.2Ag alloy. Microstructural characterization by field emission scanning electron microscopy indicated that the as-cast material consists of some $MgZn_2$ and Ag-rich MgZn precipitates. These silver-rich MgZn precipitates were entirely and partially dissolved after the solution treatment and MDF, respectively. In addition, the grain size of the as-cast alloy increased by 86% and decreased by 43% after solution heat treatment and MDF, respectively. The ultimate shear strength of the as-cast material increased by 25% and reached 149.5 MPa after MDF processing, while it did not change significantly after solution treatment. The obtained results indicated that the corrosion layer formed on the samples consists of an inner layer (magnesium hydroxide) and an outer layer (phosphate compounds). Based on the corrosion tests, it was found that solution heat treatment and MDF could significantly improve the corrosion resistance of the as-cast Mg–2Zn–0.2Ag. The corrosion resistance (R_p) obtained from the electrochemical impedance spectroscopy (EIS) test exhibited enhancements of 119% and 152% after heat treatment and MDF processes, respectively. This improvement in corrosion resistance was attributed to the higher stability of the outer layer in both solution-treated and MDF-processed samples, compared to the as-cast material. The results of cell studies also indicated a significant improvement in the cell viability of the solution-treated Mg–2Zn–0.2Ag alloy sample compared with pure Mg.

Keywords ACL screws · Biodegradable materials · Cytotoxicity · Magnesium alloys · Mechanical properties · Severe plastic deformation

1 Introduction

Magnesium alloys have gained extensive attention in recent years for making different biodegradable medical implants. For example, recently they have been introduced to make biodegradable batteries [1]. Rupture of the anterior cruciate ligament (ACL) is one of the most common injuries that happen during heavy sports activities [2]. After the surgery, the tendon graft-bone junction may be impaired because of losing bone at the interface between bone and tendon. For example, after ACL reconstruction, the estimated failure rate is still higher than 10% [2]. ACL interference screws can be used to solve this problem [3]. Recently, magnesium alloys have been used to make resorbable screws, which would not need secondary surgeries to remove them from the body after tissue regeneration. In this regard, Mg is one of the most attractive biomaterials, mainly due to its biocompatibility,

✉ Reza Alizadeh
r.alizadeh@sharif.edu

1 Department of Mateials Science and Engineering, Sharif University of Technology, Tehran, Iran

2 School of Metallurgical and Materials Engineering, College of Engineering, University of Tehran, Tehran, Iran

3 Biomaterials Research Group, Department of Materials Engineering, Isfahan University of Technology, Isfahan, Iran

4 The School of Engineering and the Built Environment, Faculty of Science and Engineering, Anglia Ruskin University, Chelmsford CM1 1SQ, UK

Published online: 23 January 2024

biodegradability, high strength-to-weight ratio, and similar mechanical properties to bone. This silvery-white metal is the fourth abundant element in the human body that stabilizes RNA and DNA. Mg also contributes to the function of more than 300 enzymes [4]. However, this light metal has some disadvantages in biomedical applications [5, 6].

Although the degradation of Mg is desirable and necessary for making resorbable implants, the degradation rate should be controlled so that it is not faster than the rate of tissue regeneration. Fast degradation of Mg in the human body is the most crucial drawback of this metal, which limits its extensive use in biomedical applications. Degradation of Mg also leads to the release of hydrogen gas, which causes toxicity and might result in severe problems for the patient [4]. Another problem is that pure Mg is usually soft for most applications [7]. Accordingly, there are some strategies to reduce the degradation rate of Mg which can also improve its mechanical properties. These strategies include methods which change chemical composition, such as alloying [8], and those that do not, such as heat treatment [9] and severe plastic deformation (SPD).

Zinc, as one of the most abundant nutritional elements in the body [10], can be dissolved into Mg up to a certain level (1.6 wt% at room temperature), resulting in solid solution strengthening [11]. Also, zinc addition improves the mechanical properties of Mg by grain refinement [12]. In addition to mechanical properties, Zn improves the corrosion resistance of Mg [12, 13]. This element helps forming a passive layer on Mg, significantly reducing the degradation rate [14]. These features and properties make Zn a desirable and exciting alloying element for magnesium alloys used or planned to be used, as resorbable implants. However, whenever zinc atoms are not in the solid solution state and form intermetallic compounds with Mg or other existing alloying elements, degradation would be locally heterogeneous, and the degradation rate can be increased due to micro-galvanic corrosion [15, 16]. Accordingly, zinc addition to resorbable magnesium alloys should be up to an optimum amount not to deteriorate the corrosion resistance. For example, it has been reported that [14] adding 2 wt% Zn to Mg exhibits the best corrosion resistance. In this regard, solution heat treatment effectively reduces localized corrosion [17].

It is worth noting that besides alloying and heat treatment, severe plastic deformation processes can also be successfully used to simultaneously improve the mechanical and degradation behavior of resorbable Mg alloys [18–20]. Among different SPD methods, multi-directional forging (MDF) shows some advantages for processing magnesium alloys, including simplicity, and more importantly, the ability to be applied directly on the as-cast alloys, while some other SPD methods such as equal channel angular pressing (ECAP) need a primary hot extrusion step. MDF is an SPD method that has been previously shown to positively affect the strength and corrosion resistance of pure Mg [21], Mg–6 wt% Zn [12], and Mg–4 wt% Zn–0.3 wt% Sr alloys [22]. Forming a stable corrosion layer on the MDF processed sample was introduced as the leading cause of the observed improvement in corrosion resistance of pure Mg [21]. Also, the barrier effect of grain boundaries against corrosion seems to play an essential role in controlling corrosion of the Mg–6 wt% Zn alloy after processing by MDF [12].

Bacterial infection is one of the most severe side effects of bone, tendon, or ligament fixation and regeneration surgeries. Therefore, the antibacterial characteristics of materials used as ACL screws are crucial. Magnesium has shown antibacterial features in in-vitro experiments, mainly due to its high degradation rate, which increases pH due to released OH^- ions [23]. However, the corrosion rate of magnesium in in-vivo environment is lower than that in the in-vitro condition due to the high level of chloride ions in in-vitro condition [24]. As a result, the antibacterial property of Mg observed in the in-vitro environment is insufficient for the in-vivo environment [25]. Some elements such as silver can improve the antimicrobial properties of Mg. It has been shown that silver in different states, such as precipitated nanoparticles and formed intermetallic compounds or being dissolved in the matrix, demonstrate antibacterial properties and affect a wide range of bacteria, including antibiotic-resistant bacteria (MRSE, MRSA bacterias) [26].

Accordingly, two strategies of heat treatment (solution heat treatment) and severe plastic deformation (MDF), which do not change the overall composition of the alloy, are used in this investigation to improve the mechanical and corrosion properties of an Mg–2Zn–0.2Ag alloy. These processes have the potential to simultaneously improve the mechanical and corrosion properties, however, with different efficiencies, which would be evaluated and compared in this investigation. Finally, the ACL screws made from this alloy are evaluated from the degradation and cell behavior viewpoints.

2 Materials and Methods

2.1 Material Preparation

Pure magnesium (99.98 wt%), zinc (99.98 wt%), and silver (99.98 wt%) were used to cast the Mg–2 wt% Zn–0.2 wt% Ag alloy. It should be noted hereafter that all compositions are in weight percent unless mentioned. An induction furnace with a graphite crucible was used for melting pure Mg at 750 °C. Zinc and silver were added to the molten Mg and mixed thoroughly. The melt was held for 10 min at 750 °C to homogenize the melt composition and then poured into a steel mold preheated to 200 °C, which yielded casting billets with dimensions of 120 mm × 40

mm × 20 mm. For simplicity, the as-cast alloy is named AC. The inductively coupled plasma (ICP) analysis evaluated the alloys composition. The ICP results indicated that AC alloy contains 0.17% silver and 1.81% zinc, being almost close to the nominal composition. Some parts of the as-cast billet were solution-treated (ST) at 400 °C for 10 h in an electrical resistance furnace and then quenched in water at 25 °C. The ACL screws were machined from both AC and ST samples.

The MDF process was carried out on AC samples with dimensions of 20 mm × 13 mm × 13 mm at 280 °C. After holding the specimen at the proposed deformation temperature for 10 min, the process was carried out in an MTS machine with a crosshead speed of 0.5 mm/min. In the first pass, as shown in [27], the sample was forged multidirectionally by exerting a compressive force on the surface A. After the first pass, the sample was rotated 90°, and then surface B was compressed. Finally, the third pass was performed by applying the compressive force on surface C. All samples were deformed for six passes. The applied strain (ε_{MDF}) on a rectangular prism specimen after each pass of MDF is calculated by the following equation [28].

$$\varepsilon_{MDF} = \frac{2}{\sqrt{3}} \ln \frac{H}{W} \tag{1}$$

where H and W are the sample height and width, respectively. Accordingly, the obtained total strain after 6 passes of MDF is about 3.

2.2 Microstructural Characterization

The microstructure of the samples was studied by the optical (OM, Olympus) and field-emission scanning electron microscopy (FESEM, TESCAN MIRA 3 LMU), using backscattered electrons and the acceleration voltage of 15.0 kV. Metallographic samples were first cut and ground up to 3000 grit. Afterward, samples were polished with 0.3 µm α–alumina slurry. The Nital solution (8-volume percent nitric acid in ethanol) was used for the AC samples. In contrast, picral solution (0.4 g picric acid, 2 ml distilled water, 6 ml ethanol, and 2.5 ml acetic acid) was used for the solution-treated and MDF-processed samples. After etching, samples were washed with ethanol and dried with warm air. The dendrite cell, volume fraction of precipitates, and grain size were measured from the optical and FESEM micrographs, using the ImageJ software. Energy-dispersive X-ray spectroscopy (EDS) was used for analyzing the composition of different phases. X-ray diffraction (XRD) analysis was conducted for phase identification in the AC and ST samples. The K-alpha copper beam was diffused in the 2θ range of 15–85° for all samples.

2.3 Mechanical Characterization

The shear punch test (SPT) was used to evaluate the mechanical behavior of the studied materials. The required samples for SPT were sliced with an electrical discharge wire cut machine to the dimensions of 10 mm × 10 mm ×1 mm. By grinding both sides of the samples to remove any oxide films, their thickness was reduced to 0.7–0.9 mm. These samples were then fixed in the SPT fixture, and the test was performed under compressive force with a constant cross-head speed of 0.25 mm/s at 25 °C in a Santam universal testing machine with a load cell capacity of 20 kN. The machine simultaneously recorded the force and punch displacement during the test, and the shear stress, τ, was calculated from the following equation

$$\tau = \frac{P}{\pi D t} \tag{2}$$

where P is the applied force, D is the average of the punch and die hole diameters, and t is the specimen thickness. The normalized displacement was derived from the punch displacement divided by the specimen thickness.

2.4 Degradation Characterization

2.4.1 Electrochemical Corrosion

The electrochemical corrosion assessment was performed on a 10 mm × 10 mm surface in a phosphate-buffered saline (PBS) solution. The composition of PBS is given in Table 1. Before testing, the sample's surface was ground up to 3000 grit and washed and dried with ethanol and a warm air stream, respectively.

Three-electrode configuration was used to perform the potentiodynamic polarization and the electrochemical impedance spectroscopy (EIS) tests. The specimen, Ag/AgCl, and platinum plate were used as the working, reference, and counter electrode. In the polarization test, the voltage range and the scan rate were ± 250 mV and 1 mV/s, respectively. Tafel extrapolation was used to obtain the corrosion potential (E_{corr}) and corrosion current

Table 1 Chemical composition of the used PBS solution

Composition	Concentration (g/liter distilled water)
NaCl	8.00
KCl	0.20
Na_2HPO_4	1.15
K_2HPO_4	0.20

density (i_{corr}). The EIS test was run with a 10 mV amplitude and a frequency range of 100 mHz–10 kHz.

2.4.2 Immersion and Hydrogen Evolution Tests

Samples with an approximate area of 100 mm^2 were ground up to 3000 grit, washed carefully by ethanol and dried with warm air, and then immersed in PBS at 37 °C. The produced hydrogen gas during immersion was collected using a system including a funnel and a burette. The immersion test continued for 264 h (11 days), and the produced hydrogen level was recorded at 24 h intervals. FESEM investigated the morphology of the corroded samples. In addition to immersion tests on bulk samples, the appearance of the ACL screws after soaking in the PBS solution at 37 °C for 264 h was also studied by FESEM.

2.5 Biological Evaluations

2.5.1 Cell Culture and Cytotoxicity Assay

Fibroblast cell line- L929 was cultured in Dulbecco's Modified Eagle Medium (DMEM) supplemented with 10% fetal bovine serum, 100 U/mL penicillin, and 100 g/mL streptomycin for 3 days at 37 °C with every other day's culture medium being changed. The samples (pure Mg as the reference material and solution-treated Mg–2Zn–0.2Ag alloy) were placed in a 24-well plate in triplicates and sterilized using a UV light for 20 min on each side followed by three times washing with PBS prior to being submerged in culture media overnight. Cells were seeded at a density of 3×10^3 cells per sample, and tissue culture polystyrene (TCP) and cell viability assay were conducted after 24, 48, and 72 h.

Alamar blue (Invitrogen, UK) cell viability assay was performed according to our previous study [29]. At the end of each time point, each well was washed with PBS, then covered with 500 µl of Alamar blue solution (1:10 culture media: Alamar blue reagent) and incubated for 2 h. The optical density was measured at 570 nm using a microplate reader (BioTek, FLX800).

2.5.2 Cell Attachment

Cell attachment on the surface of each sample was evaluated using scanning electron microscopy (SEM, Philips XL30). Cell-seeded constructs were retrieved after 48 h of incubation to study the cells' morphological traits. Cell-cultured samples were briefly washed in PBS, fixed for 2 h in 2.5% glutaraldehyde, rinsed in distilled water, and dehydrated using a graduated series of ethanol solutions (60% up to 100% [v/v]). Gold-sputtered specimens were then visualized using SEM.

3 Result and Discussion

3.1 Microstructural Characterization

The general optical microstructure of the alloy in different studied conditions of AC, ST, and multi-directionally forged are presented in Fig. 1. The typical dendritic structure of the AC alloy (Fig. 1a) has been vanished after the solution treatment (Fig. 1b). The average dendrite cell size of the AC alloy is around 31.1 µm, while the average grain size of the ST alloy is obtained to be 57.8 µm. The microstructures of the MDF-processed alloy at two magnifications are shown in Fig. 1c and d. The average grain size of the MDF-processed specimen was found to be about 17.8 µm, which shows about a 43% reduction in comparison with the average dendrite cell size of the AC condition. For a more straightforward comparison, the grain size distribution histograms of the ST and MDF specimens are shown in Fig. 1e and f, respectively. The ST specimen has an unimodal grain size distribution within a narrow range of grain sizes (0-170 µm). The grain size distribution of the MDF processed sample, together with the small standard deviation value of 11.2 µm, indicate the formation of a homogenous fine-grain microstructure after MDF.

The FESEM micrographs of the AC alloy are shown in Fig. 2a–c. Figure 2a shows that zinc-rich particles can be found at dendrite cell boundaries and inside dendrite cells, where the volume fraction of the precipitates was estimated to be around 7.5 ± 0.5%. According to the EDS analysis (Fig. 2h) taken from one of these white particles (area 1 in Fig. 2b), the atomic ratio of Mg to Zn is close to that anticipated for the MgZn precipitates. Therefore, these precipitates are most likely MgZn secondary phases, with some silver incorporated in their structure. This observation is in agreement with that reported in [30], where Ag was merged in the Mg-Zn precipitates in an Mg–0.5Zn–0.2Ag alloy. The EDS results (Fig. 2h) from area number 2 in Fig. 2b show that such regions are solid solutions of Zn and Ag in Mg (α-Mg). In addition to these microstructural features, some fine precipitates also exist in the AC alloy, where one of these precipitates is shown in Fig. 2c. The dimension and morphology of these particles are similar to those anticipated for the blocky $MgZn_2$ precipitates. The presence of these precipitates in the as-cast Mg–Zn based alloys has been reported before [31]. Besides the as-cast microstructures, the existence of $MgZn_2$ precipitates in the aged Mg–4Zn [27] and Mg–Zn–Mn [32] alloys, has been also reported.

The microstructure of the ST specimen is presented in Fig. 2d and e, indicating the formation of an almost single-phase microstructure after solution treatment. Volume fraction of the remained precipitates was estimated to be

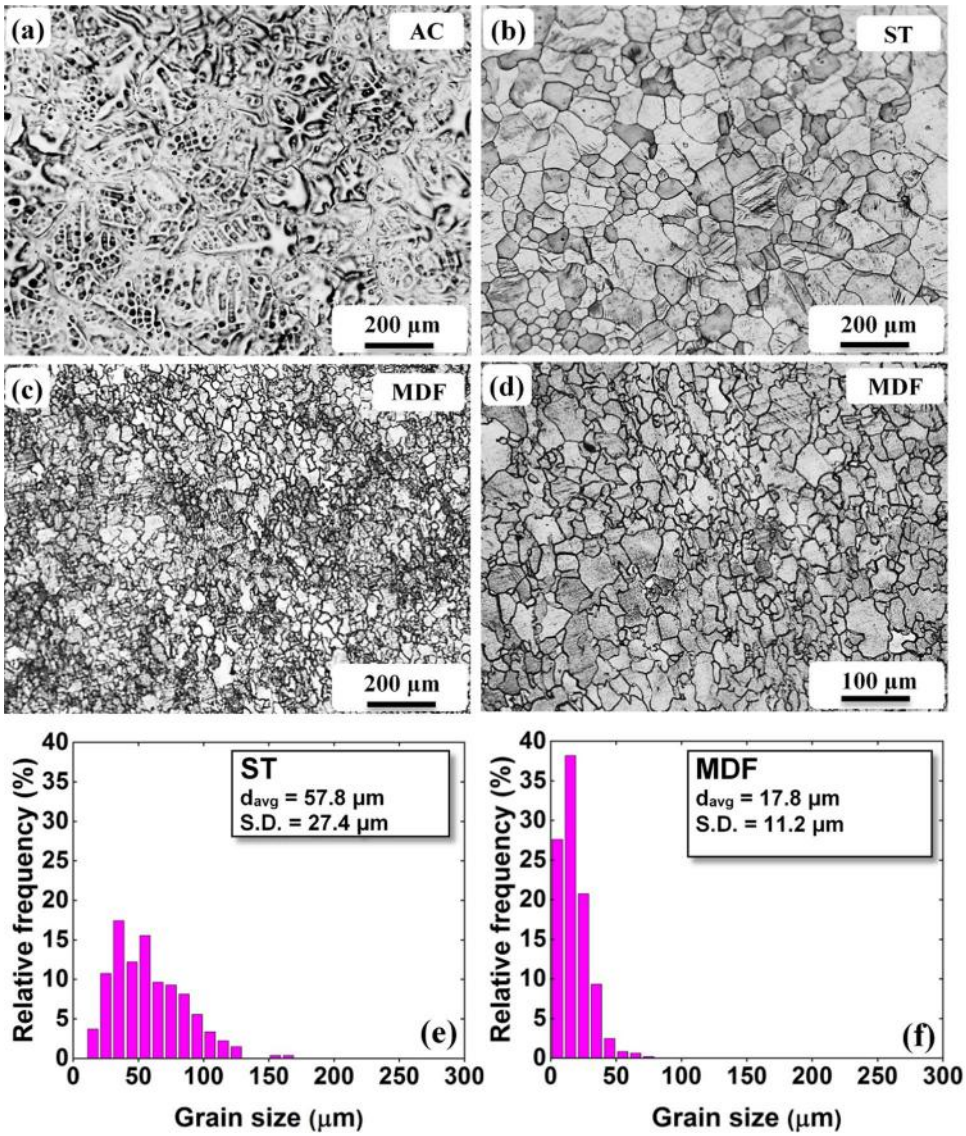

Fig. 1 Optical microstructures of the Mg–2Zn–0.2Ag alloy in different states: AC (**a**), ST (**b**), and MDF (**c**, **d**). Grain size distribution histograms of the alloy in the ST and MDF states are also given in (**e**) and (**f**), respectively

only 0.4 ± 0.1%. This phase should be a super-saturated solid solution of Ag and Zn in Mg. However, some small sparse secondary phases could still be detected in some parts of the microstructure, as shown in Fig. 2e. Considering the Mg–Zn phase diagram [11] and also the precipitates in the AC alloy; it is inferred that these particles with excellent thermal stability at 400 °C should be $MgZn_2$. The melting point of the $MgZn_2$ phase is about 595 °C, the highest of all possible intermetallic compounds in the Mg–Zn alloy system. Previous works have reported similar results on the as-cast [33] and extruded [34] Mg–4Zn alloy. Finally, Fig. 2f illustrates the microstructure of the MDF-processed specimen, where a uniform fine-grained microstructure has been obtained. It can be observed that conducting the MDF process at 280 °C has dissolved most of the precipitates, and thus, a quasi-single phase structure has been obtained. In fact, the volume fraction of the precipitates is decreased from the initial value of 7.5 ± 0.5% in the as-cast condition to 0.6 ± 0.2% after MDF. This effect can indicate MDF-stimulated solution treatment. A similar effect was observed in an Mg–6Zn alloy processed by equal channel angular pressing (ECAP), another severe plastic deformation process. It was observed that an almost single-phase microstructure could be achieved by performing six passes of ECAP at 320 °C [35]. However, some Zn and Ag-rich precipitates can be detected in the microstructure of the MDF-processed alloy, where one of them is shown at higher magnification in Fig. 2g. The EDS results obtained from this small particle (Fig. 2h) can be associated with some degrees of inaccuracy, but indicates that it contains some Ag and Zn.

Figure 3 shows the XRD spectrum of the AC and ST specimens. Peaks of the α-Mg and MgZn phases are detected in the spectrum of the AC specimen. However, obviously

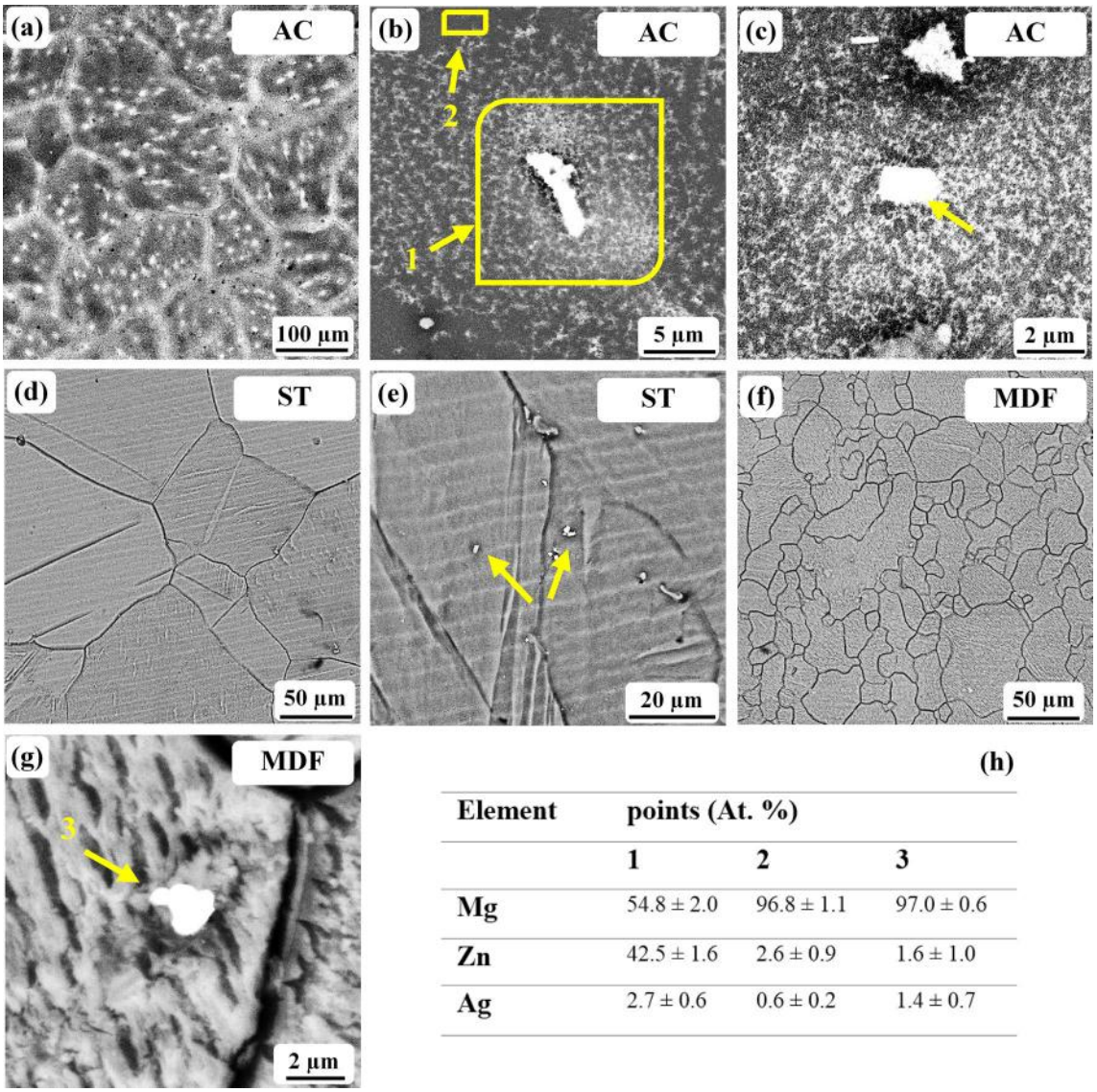

(h)

Element	points (At. %)		
	1	2	3
Mg	54.8 ± 2.0	96.8 ± 1.1	97.0 ± 0.6
Zn	42.5 ± 1.6	2.6 ± 0.9	1.6 ± 1.0
Ag	2.7 ± 0.6	0.6 ± 0.2	1.4 ± 0.7

Fig. 2 FESEM micrographs of the Mg–2Zn–0.2Ag alloy in different states: AC (**a**-**c**), ST (**d**, **e**), and MDF (**f**, **g**). The EDS results of selected points are also given in (**h**)

and per the FESEM results, peaks related to the MgZn precipitates have been diminished after solution treatment. It is worth noting that the $MgZn_2$ peaks could not be detected in the spectrums, which is related to the low volume fraction of this phase.

3.2 Mechanical Properties

Figure 4a exhibits shear stress vs. normalized displacement curves of the AC, ST, and MDF-processed specimens. Figure 4b represents ultimate shear strength (USS) and shear yield strength (SYS) values derived from the curves presented in Fig. 4a. As can be observed, the SYS values for the AC and the ST specimens are almost equal. However, the USS value of the ST specimen is slightly higher than the AC alloy. The mechanical strength of the solution-treated alloy would be a balance between losing strength due to grain growth and precipitate dissolution [36] and gaining strength from the solid solution strengthening mechanism. Hence, solution treatment can decrease or increase the mechanical strength depending on the domination of the above-mentioned influencing factors. No considerable change in strength level was observed after the solution treatment of the as-cast Mg–2Zn–0.2Ag alloy at 400 °C for 10 h.

Comparing the AC and MDF curves, it can be deduced that the MDF process generally results in strengthening, where the SYS of the MDF specimen has increased by 16%, compared to the AC specimen. This strengthening

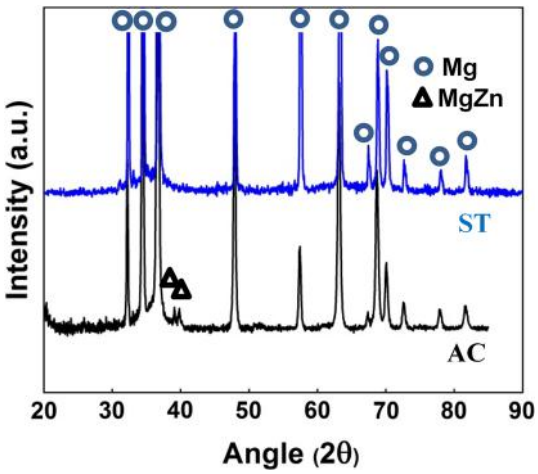

Fig. 3 XRD patterns of the AC and ST samples

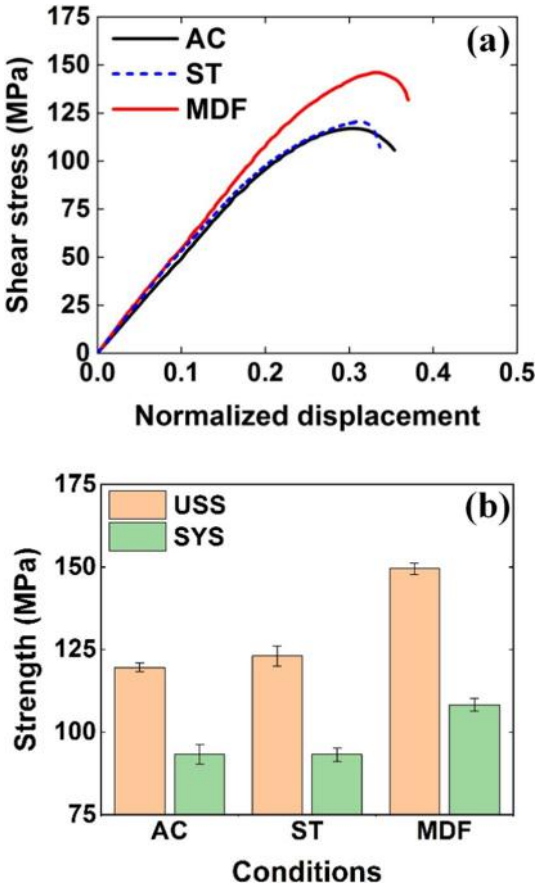

Fig. 4 (**a**) SPT curves of the Mg–2Zn–0.2Ag alloy in different states. The SYS and USS values are summarized in (**b**)

mainly originates from the fine microstructure of the MDF-processed specimen, as indicated before. In this regard, it should be noted that the yield strength of a metal is inversely related to grain size according to the well-known Hall-Petch equation [37]. Indeed, the K_y value (locking parameter, a measure of the relative hardening contribution of grain boundaries) of the Hall-Petch equation for metals with hexagonal closed packed (HCP) structure is more significant than that of the metals with face-centered cubic (FCC) structure. As a result, the impact of microstructure refinement on the mechanical strength of HCP metals such as magnesium is more significant than FCC metals [37].

The USS values of the AC and the MDF-processed specimens were obtained to be 119.6 and 149.5 MPa, respectively, corresponding to a 25% increase. This increase is in accordance with our previous work on the Mg–4Zn–0.3Sr alloy, where the USS of the as-cast alloy was increased by 11% after the MDF process [22]. This strengthening effect, together with the observed improvement in ductility and toughness, indicates the MDF process's suitability for improving the mechanical properties of resorbable Mg–Zn alloys. The importance of this enhancement becomes clearer, considering that ACL screw head breakage during the surgical insertion of the screw, is one of the most challenging issues affecting the clinical use of Mg-based interference screws. As a result, improving strength is vital for magnesium alloys making ACL screws [2].

3.3 Corrosion Properties

3.3.1 Corrosion Morphology

Figure 5 shows FESEM corrosion morphologies of the material in the AC, ST and MDF states, all taken after 11 days of immersion in the PBS solution. The EDS results obtained from surface films are also displayed in Table 2. Some broad and large cracks can be seen on the corroded surface of the AC alloy (Fig. 5a). Figure 5b is related to the corroded surface of the ST specimen. Some cracks are also visible on the surface of this sample, though they are much thinner and smaller in length than those on the surface of AC specimen. The corroded surface of the MDF specimen is also shown in Fig. 5c. Here, cracks are much more minor in size than the AC and ST specimens. In addition, EDS analysis (Table 2) obtained from regions B and C in Fig. 5b and c, respectively, show almost similar compositions to that obtained for the AC alloy (region A), except that higher zinc and phosphorous contents are found in regions B and C compared to region A. Therefore, phosphate compounds in the ST and MDF specimens are more likely similar to the AC specimen.

Figure 5d and g present the cross-section FESEM microstructure of the AC specimen at low and high magnifications, respectively. According to these figures, the progress of the corrosion process is heterogeneous, which results in the pitting of some areas. One of these pits can be seen in Fig. 5a, indicated by a white arrow. EDS analysis was performed on different areas of Fig. 5g, and the results are

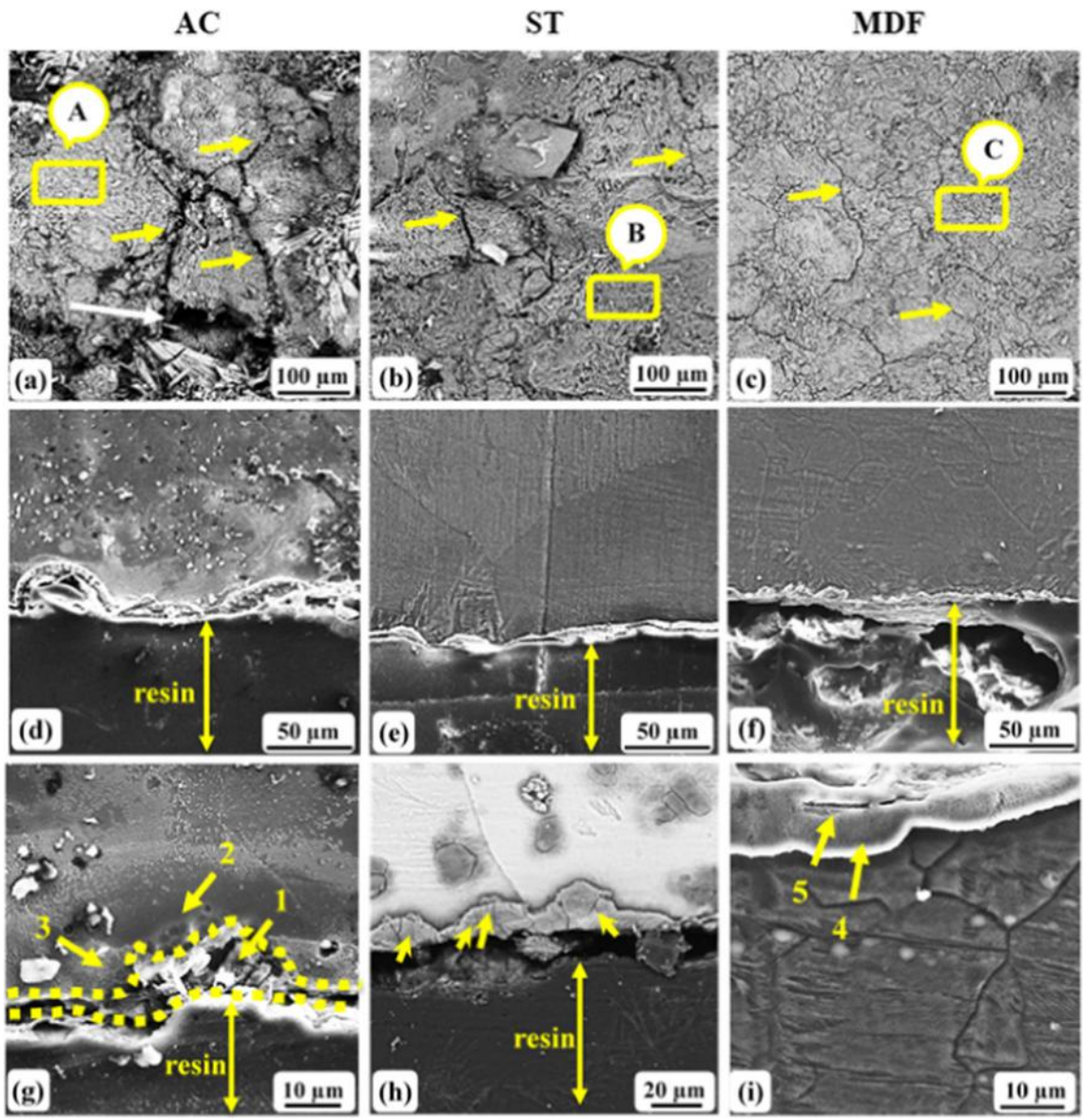

Fig. 5 FESEM micrographs showing the corrosion morphology of the Mg–2Zn–0.2Ag alloy in different states of AC (left column), ST (middle column), and MDF (right column). The first row shows top views, while the second and third rows show cross-sectional views. The EDS results obtained for regions *A* (**a**), *B* (**b**) and *C* (**c**) are presented in Table 2

Table 2 EDS results of selected areas shown in Fig. 5

Element	Regions (At%)							
	A	B	C	1	2	3	4	5
Mg	27.4 ± 1.2	28.6 ± 4.6	26.8 ± 2.5	29.2 ± 0.2	99.7 ± 1.3	97.6 ± 1.8	31.7 ± 6.9	27.0 ± 4.2
O	69.6 ± 3.1	65.9 ± 4.6	67.4 ± 2.3	67.2 ± 0.9	–	–	65.4 ± 1.1	59.2 ± 0.4
P	2.8 ± 0.6	4.2 ± 1.8	4.0 ± 0.6	3.4 ± 0.6	–	–	2.9 ± 0.7	13.5 ± 1.4
K	0.1 ± 0.1	0.1 ± 0.1	0.1 ± 0.1	0.1 ± 0.1	–	–	0.1 ± 0.1	0.1 ± 0.1
Zn	0.1 ± 0.1	1.2 ± 0.4	1.8 ± 0.2	0.1 ± 0.2	0.3 ± 0.2	1.9 ± 0.2	0.1 ± 0.1	0.2 ± 0.1
Ag	–	–	–	–	–	0.5 ± 0.1	–	–

summarized in Table 2. The results show that region 1, the area between two dashed lines, should be the surface corroded film. It is also evident that region 3 has a higher zinc and silver content than region 2. Therefore, micro-galvanic corrosion can occur between areas with different chemical compositions, including regions 2 and 3 in Fig. 5g, which causes severe corrosion in more active areas.

Figure 5e shows the cross-sectional FESEM microstructure of the corroded ST specimen. In contrast to the AC specimen, corrosion process in the ST specimen seems more homogenous. Small cracks in the surface film of this specimen, marked by small yellow arrows, are shown at a higher magnification in Fig. 5h. It is worth noting that these cracks are grown into a high depth in the corrosion film, as cross-sectional micrograph demonstrates. Therefore, the probability of the formation of these cracks as a result of the dehydration phenomenon by FESEM is low.

Cross-sectional FESEM micrographs of the corroded MDF-processed specimen are shown in Fig. 5f and i. Compared to the AC specimen, the degradation process of this specimen has occurred more homogeneously, as inferred from the occurrence of less pitting on the surface of this specimen. Indeed, the micro-galvanic effect has not occurred significantly in this specimen, due to the more homogenous microstructure of this material with fewer precipitates than the AC specimen, as indicated previously in the microstructural characterization part. To further evaluate the chemical composition of the surface corrosion film, EDS analysis data collected from points 4 and 5 are given in Table 2. The obtained results indicate that region 4 is enriched in magnesium and oxygen, and thus, it should be placed in the inner layer. However, region 5 is placed in the outer layer, since it contains magnesium, oxygen, phosphorus, potassium, and zinc elements. In addition, cracks seen in Fig. 5c are not visible in the cross-sectional micrograph of Fig. 5i. Cracks in Fig. 5c can be related to the phenomenon of dehydration caused by the FESEM chamber's vacuum. Therefore, observation of cracks in the surface film of the MDF specimen should be rare, which indicates well compactness of this film.

Cross-sectional and normal views of the AC specimen together with the EDS line-scan results are presented in Fig. 6a and b, respectively. EDS Line-scan results of the corroded surfaces are shown in Fig. 6c and d. Also, Fig. 6e is an enlargement of Fig. 6c. It is obvious that the surface film formed on the AC alloy consists of two layers (Fig. 6b). According to the EDS analysis in Fig. 6d and e, the inner layer is enriched in magnesium and oxygen elements, while the outer layer is enriched in magnesium, oxygen, phosphorus, and zinc. Therefore, the inner and outer layers mostly contain magnesium hydroxide and phosphate compounds.

EDS line-scan results obtained from the top view (Fig. 6b) are presented in Fig. 6d. A considerable change in chemical composition can be observed by moving from the dark to the bright region. The dark region contains mainly magnesium and oxygen, while the bright region contains magnesium, oxygen, zinc, and phosphorus. Therefore, the inner and outer layers are the dark and bright regions. The microstructure in Fig. 6b shows that some surface areas have only one layer (bright regions corresponding to the inner layer). In contrast, in other areas, the outer layer is not broken; thus, only this layer can be observed. Region D in Fig. 6b shows the existence of porosity in the inner layer, indicating the low compactness of this layer.

To further analyze the surface chemistry of the corroded samples, the ATR-FTIR was performed, and the obtained spectrums are presented in Fig. 7. Two observed valleys at 1050 cm^{-1} and 560 cm^{-1} positions are related to the v3 and v4 vibration modes in the phosphate ions [4]. The valley at 1600 cm^{-1} is for the water molecules' vibration [38], and finally, the hydroxide ions have made a valley at 710 cm^{-1} [38], which probably corresponds to the magnesium hydroxide. These results further approve the above discussions on the nature of the corrosion films formed on the studied materials. In addition, spectrums of the alloy in different states of AC, ST, and MDF differ from some points of view. The phosphate valleys of the ST and MDF-processed specimens are sharper than the AC ones. Hence, the corroded surfaces of the MDF-processed and ST samples possess higher amounts of phosphate compounds in comparison with the AC material. As shown previously by the FESEM micrographs, the outer corrosion layer of the AC alloy had entirely broken in some areas after 11 days of immersion. However, the degradation of the surface film in the ST and MDF-processed specimens was less severe. Consequently, the IR beam has conducted more detection from the inner corrosion layer of the AC specimen, which contains fewer phosphate compounds compared to the outer layer. Instead, the hydroxide valley of the AC specimen is sharper than the ST and MDF specimens.

The FESEM macro and micrographs of the made ACL screws are shown in Fig. 8, taken before (Fig. 8a and b) and after (Fig. 8c-l) immersion in the PBS solution for 11 days. Fig. 8c-g are related to the corroded AC screw. According to Fig. 8c, corrosion severity is not macroscopically homogenous throughout the screw. While some parts of the screw are severely corroded and covered by massive corrosion products (region E), corrosion severity is much less or even negligible in other areas such as region F. As shown in Fig. 8d, corrosion severity can even be heterogeneous from one thread to another. In this regard, it can be observed that one of the threads has been totally degraded (the left thread in Fig. 8d), but the other threads (Fig. 8e) have almost completely maintained their shape details. The morphology of the corrosion film is shown in Fig. 8f at a higher magnification, where large and interconnected cracks

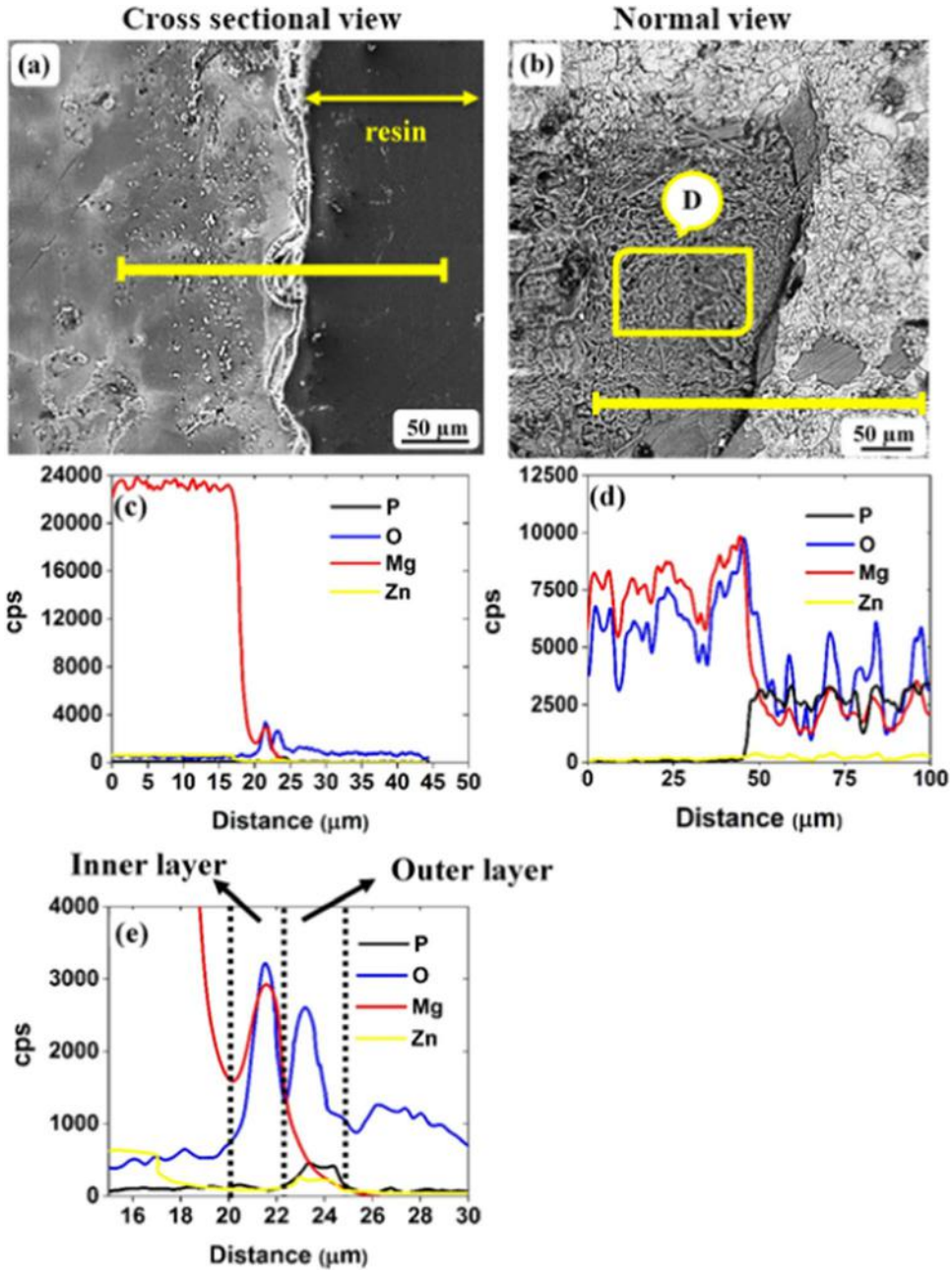

Fig. 6 EDS line-scan results obtained from the cross-sectional (left column) and top (right column) views of the AC alloy, after immersion in PBS for 264 h

can be observed. Furthermore, it can be observed that the corrosion film is broken in some parts, as indicated by the yellow arrow. Therefore, it can be concluded that the surface film of the AC screw has low stability and compactness, which results in severe corrosion of the material in a heterogeneous manner. This phenomenon can be related to severe micro-galvanic corrosion in the AC material, as indicated before, resulting in the formation of enormous pits. The yellow arrow in Fig. 8c shows a large pit on the AC screw. Figure 8g is also related to the cross-sectional view of a thread, which clearly shows the formation of pits on the corroded surface of the screw.

It would be interesting to compare the appearance of the corroded screws made from the same alloy in the AC (Fig. 8c-g) and ST (Fig. 8h-l) states. According to Fig. 8h-j, unlike the AC screw, it seems that the corrosion film is more uniformly formed and bonded to the surface of the ST screw. Figure 8k shows the surface of a thread in a closer view, where some small cracks can be observed on the thread (yellow box). These cracks are smaller than the cracks observed on the AC screw (Fig. 8f). According to Fig. 8l, which shows cross-sectional view obtained from one of the threads in the corroded ST screw, the corrosion process seems to be very uniform in this sample. There are no pits on the screw

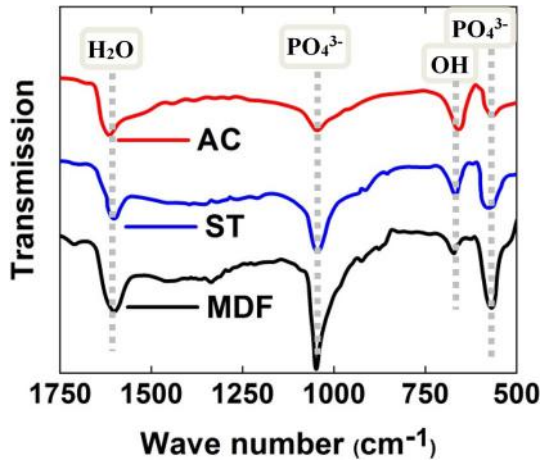

Fig. 7 ATR-FTIR spectra of the Mg–2Zn–0.2Ag alloy in different states of AC, ST, and MDF

surface. Controlling the degradation rate of the ACL screws is vital. In this regard, it has been reported that the high degradation rate of the screws causes a decreased fixation strength of the tendon graft, and finally, the surgery will fail [2]. Accordingly, performing a simple solution treatment step on as-cast alloys benefits the ACL screws and can significantly decrease the degradation rate and make the process more uniform.

3.3.2 Immersion and Hydrogen Evolution Test

Immersion tests were performed for up to 264 h on different samples (AC, ST, and MDF) to better understand the long-term behavior and the differences. By collecting and measuring the evolved hydrogen gas, hydrogen evolution curves were obtained for each sample, presented in Fig. 9a. Instantanious hydrogen evolution rates could also be obtained from such curves, which are shown in Fig. 9b. In general, it can be observed that from the viewpoint of both the amount and rate of hydrogen evolution, the studied materials can be ordered as AC > ST > MDF.

In Fig. 9b, three different regions can be distinguished in all studied materials, corresponding to different degradation mechanisms. Because of the formation of the surface film, the rate of hydrogen evolution is downward in region I. The formed surface film becomes thicker and more complete (covering more areas) by increasing the immersion time. Region II is related to the corrosion rate stabilization phase in which the surface film is completely formed and can effectively inhibit corrosion. Finally, in region III, the hydrogen evolution rate starts to be upward, and thus the degradation rate becomes unstable. The existence of region III can be originated from the cracking of the surface film, which is consistent with the FESEM micrographs obtained from corroded samples (Fig. 5a–c). According to Fig. 9b, it is observed that the stability stage (region II) is more extended for both ST and MDF samples compared to the AC alloy.

3.3.3 Electrochemical Corrosion

The potentiodynamic polarization curves of the alloys are shown in Fig. 9c. The $E_{corr,}$ and i_{corr} values were obtained from the intersection of the anodic and cathodic Tafel lines and are summarized in Fig. 9e. According to Eq. 3 [39],

$$p_i = 22.85 i_{corr} \tag{3}$$

the corrosion rate of each sample, p_i (mm/year), can be calculated from the given i_{corr} (mA/cm^2) values. The corrosion rate values are also presented in Fig. 9e.

By comparing the corrosion rate values, a similar trend to that obtained from the hydrogen evolution curves is revealed; the MDF and AC specimens have the best and worse corrosion resistance, respectively. In addition, as can be observed in Fig. 9c, the anodic branch of the AC alloy has a breakdown point, indicated by a small arrow. This sudden change in the anodic branch slope demonstrates the tendency of localized corrosion and breakdown of the surface film [39, 40], which is consistent with the FESEM micrographs of the corroded samples (Fig. 5a and g). By comparing the obtained results from the hydrogen evolution and polarization tests, it is found that the difference in degradation behavior of the AC and ST samples is more pronounced and best revealed in the hydrogen evolution test. The polarization test cannot evaluate the in-vitro corrosion behavior of Mg alloys, and behavior originated from the negative difference effect (NDE) of the polarization test [41]. By increasing the applied potential in the polarization test, the hydrogen evolution and magnesium degradation reactions occur at a higher rate than expected [42]. Therefore, the theoretical and experimental errors of the hydrogen evolution method are less than the electrochemical test [43].

Figure 9d illustrates the Nyquist plots of the materials along with the fitted equivalent circuit. The Nyquist diagrams consist of two loops in high and medium frequencies. The loops at high and medium frequencies are related to the electric double layer and corrosion film properties, respectively [44]. It can be readily observed that while the general shape of the loops is the same for all three specimens, their size is different. Therefore, the corrosion mechanism of all three samples should be similar, as will be discussed in more detail in the following section, but their corrosion resistance is different [45].

Figure 9e demonstrates the equivalent circuit parameters, where R_S is the solution resistance unrelated to the alloys' corrosion properties, and CPE_1 and R_1 are the electric double-layer capacitance and charge transfer resistance, respectively [44]. It is worth noting that

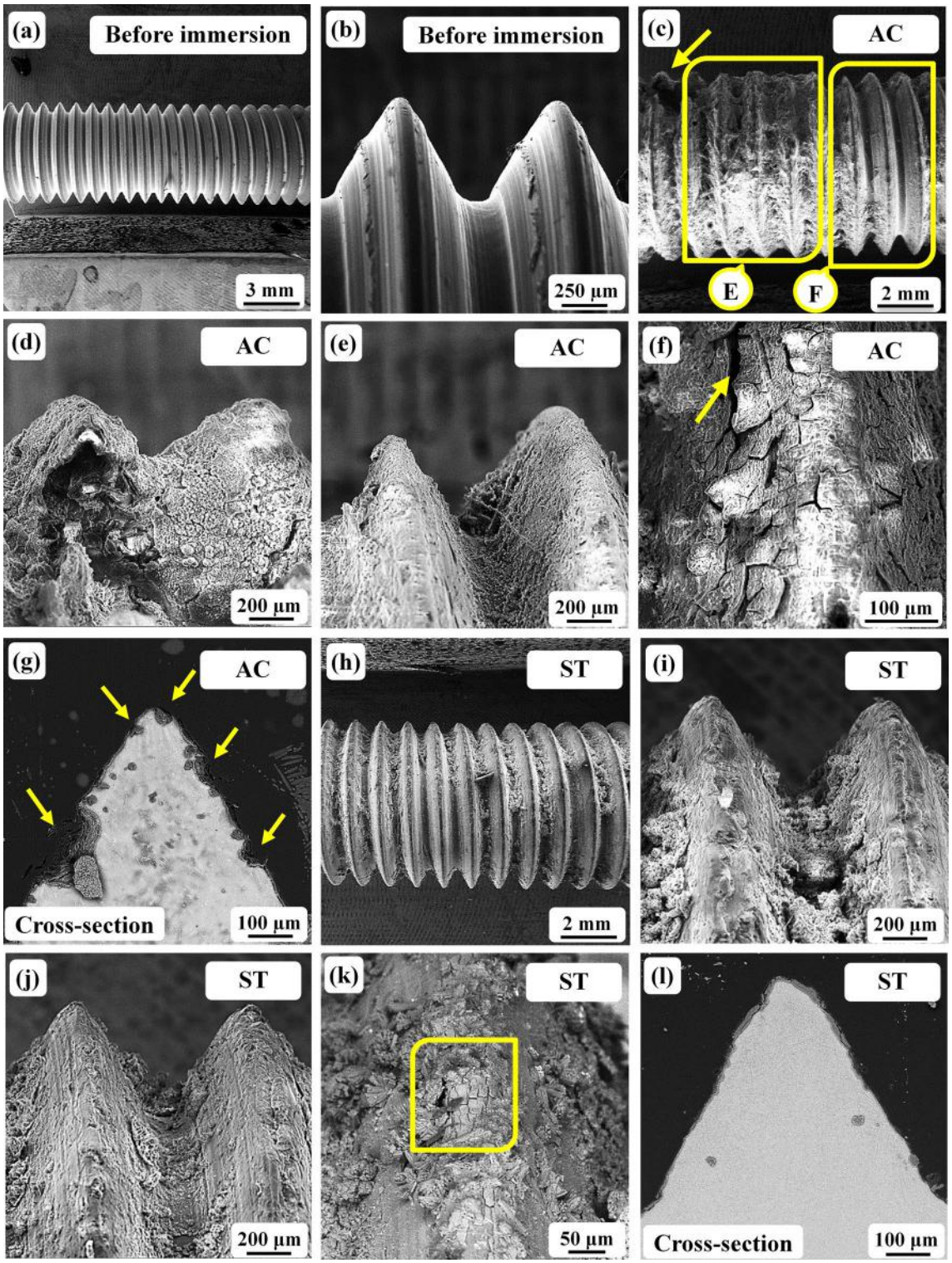

Fig. 8 FESEM micrographs showing the appearance of the ACL screws both before (**a**, **b**) and after (**c**–**l**) immersion. A comparison is also made between screws made from the AC (**c**–**g**) and ST Mg–2Zn–0.2Ag alloy

the constant phase element (CPE) explains the non-ideal capacitor behavior. Some factors, such as surface roughness, electrode surface porosities, and potential and current distribution heterogeneity, cause this deviation [38]. CPE_2 and R_2 are also the capacity and resistance of the surface film and show the mass transfer behavior

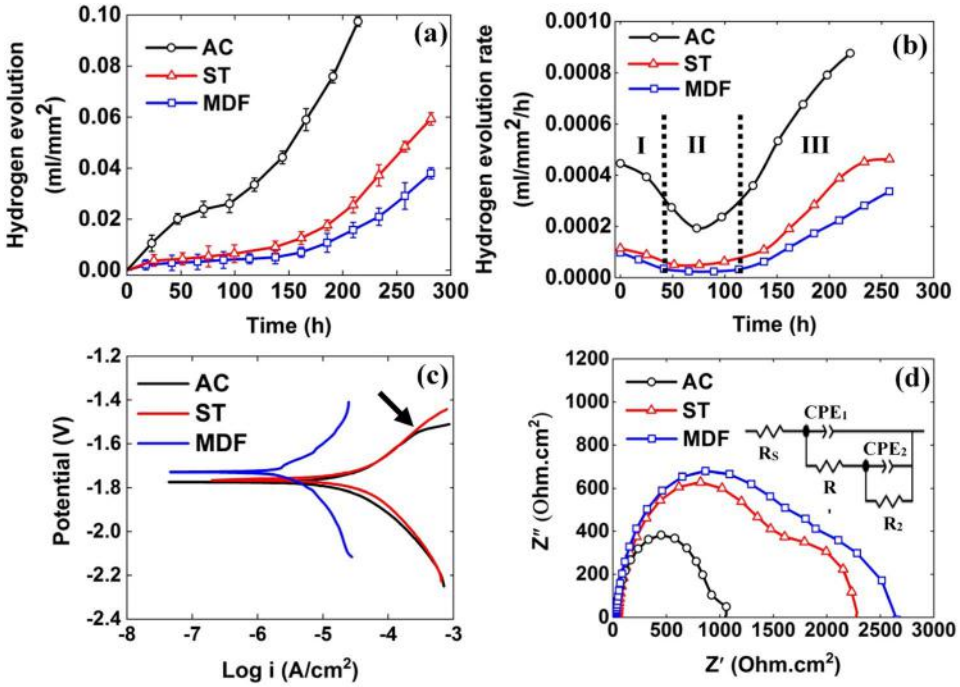

Fig. 9 Corrosion tests results: Hydrogen evolution vs. immersion time curves (**a**), hydrogen evolution rate vs. immersion time curves (**b**), potentiodynamic polarization curves (**c**), Nyquist plots and the equivalent circuit (**d**). The corrosion data extracted from the polarization and Nyquist curves are summarized in (**e**)

(e)

Alloy state	E_{corr} (V)	i_{corr} (μA/cm²)	R_i (mm/y)	R_S (Ω.cm²)	CPE_1 ($\Omega^{-1}.cm^{-2}.s^n$)	R_1 (Ω.cm²)	CPE_2 ($\Omega^{-1}.cm^{-2}.s^n$)	R_2 (Ω.cm²)	R_P (Ω.cm²)
AC	-1.774	3.910	0.0880	24	2×10^{-7}	870	2.5×10^{-5}	150	1020
ST	-1.766	2.070	0.0473	25	1.5×10^{-7}	1500	1.4×10^{-5}	730	2230
MDF	-1.729	0.820	0.0187	22	1.3×10^{-7}	1525	1.3×10^{-5}	1050	2575

[44]. When the charge transfer resistance is significant, the transfer of electrons is complex, and thus the corrosion resistance is improved [46]. Furthermore, surface film resistance (R_2) is also directly related to corrosion resistance. Hence, the sum of the two resistances (R_1 and R_2) is equivalent to the overall corrosion properties of the alloy, which is the polarization resistance (R_p) [34]. From the polarization resistance values of the specimens given in Fig. 9e, it is evident that the same order observed in the hydrogen evolution and polarization tests are applicable here. The double-layer capacitance is inversely related to the film thickness [44].

In another research [3], two different screws made of Mg–6Zn–0.5Sr alloy and Polylactic acid (PLA) were evaluated and compared. After 6 and 16 weeks of in-vivo experiments, histological investigation revealed that the Mg–6Zn–0.5Sr screw was suitable for this application and had higher bone growth in the peri-tunnel region than the PLA one. Also, the corrosion current density of the Mg–6Zn–0.5Sr alloy was obtained to be about 2.98 μA.cm^{-2}, which is higher than the ST and MDF samples studied in this investigation (2.07 and 0.82 μA.cm^{-2}, respectively).

3.3.4 Corrosion Mechanisms

According to the obtained results in this investigation, and also, those reported in previous related works, the following corrosion mechanism can be considered:

Step 1 When the alloys are immersed in the PBS solution, according to reactions 4 and 5, hydrogen gas, together with magnesium and hydroxide ions is produced. As the immersion time increases, the concentration of hydroxide ions in the solution rises, and thus, the pH of the solution would be increased. The magnesium hydroxide ($MgOH_2$) precipitates on the surface of alloys due to the solution's increasing pH [47, 48]. With increasing immersion time, thickness of the corrosion film increases, and the corrosion rate declines [49]. The formation of magnesium hydroxide on the surface of different magnesium alloys immersed in the PBS solution has been extensively reported in the literature [34, 38, 44, 46, 50–53]. As shown in Fig. 6, this $Mg(OH)_2$ film protects the underlying alloy inadequately, because of too many porosities in the corrosion layer.

$$Mg \rightarrow Mg^{2+} + 2e^- \quad (4)$$

$$2H_2O + 2e^- \rightarrow 2OH^- + H_2 \quad (5)$$

On the other hand, the chloride ions, with a radius of 0.181 nm, are one of the smallest ions in the PBS solution, which has a high diffusion rate. The presence of chloride ions in the PBS solution at a concentration higher than 150 mmol/l causes considerable diffusion of this ion through pores of the magnesium hydroxide layer, converting magnesium hydroxide to magnesium chloride [54]. The precipitated magnesium chloride is highly soluble and dissolves in the PBS solution. Hence, a new magnesium surface would be exposed to the PBS solution. As a result, the protectiveness of the formed magnesium hydroxide layer in step 1 is insufficient. The chloride ion concentration in the PBS solution used in this study is about 140 mmol/l, which is close to the mentioned critical value.

Step 2 After forming the magnesium hydroxide layer, the outer layer with higher concentrations of Zn, Mg, and phosphor is formed, in agreement with the results presented and discussed before (Figs. 6 and 7). Due to the presence of a considerable amount of phosphate ions in the used PBS solution (about 9.3 mmol/l), there is a high possibility of forming phosphate compounds in the outer layer. The presence of these different compounds in the corrosion film can significantly influence the corrosion performance, which has been extensively referred to and discussed in the literature [34, 38, 50, 53, 55–57]. For example, it has been reported that the corrosion layer formed on a WE43 alloy in a NaCl-containing solution was only magnesium hydroxide. However, when the alloy was immersed in a NaCl+K_2HPO_4 solution, phosphorus, carbon, oxygen, and magnesium elements were detected in the corrosion layer, indicating the formation of phosphate compounds in the film [56]. In another investigation, increasing the concentration of the HPO_4^{2-} ions in the PBS solution resulted in less severe degradation of the AZ31B alloy. This effect was attributed to the passive layer's magnesium hydroxide and magnesium phosphate [53]. In addition, the corrosion resistance of an AZ91 alloy was improved in a solution containing HPO_4^{2-} because of the magnesium phosphate formation on the AZ91 surface [49]. It is worth noting that passivation behavior in magnesium alloys can be promoted in the presence of elements such as aluminum, yttrium, calcium, and copper [52, 57]. In addition to these elements, Zn plays a critical role in forming the passive layer. According to the EDS point- and line-scan results (Fig. 6 and Table 2), the outer layer is enriched in zinc, which demonstrates the presence of this element in the phosphate compounds. In a previous study on an Mg–4Zn alloy, magnesium hydroxide and zinc-containing phosphates in the corrosion film were reported to improve the corrosion resistance [34]. Zinc has been reported to form a stable and thick film on the Mg implants [34] and increases the adhesion of the surface corrosion layer to the substrate [40].

The higher corrosion resistance of the ST alloy compared to the AC alloy could be originated from the influence of solution heat treatment on the as-cast microstructure. A typical AC microstructure contains different kinds of heterogeneities, while the most pronounced one can be the presence of secondary phases [58]. In this investigation, it was observed that by conducting solution treatment at 400 $^{\circ}$C, most of the precipitates were dissolved in the matrix, and the microstructure became homogenous. In addition, the segregation of alloying elements and the dendritic nature of the as-cast microstructures would also disappear after solution treatment. The existence of cathodic secondary phases causes the corrosion process to be started sooner and more severely in the adjacent magnesium matrix. Hence, the electrons would transfer from the anodic to the cathodic areas. Thus, the corrosion film formed on the anodic areas will be thicker than those on the cathodic areas. Consequently, a heterogenous surface film will be formed. In a previous work on the WE43 and ZE41 alloys [38], magnesium hydroxide was detected in areas around the cathodic phases, indicating the occurrence of the micro-galvanic corrosion. In addition to this effect, the precipitates create some active sites on the corrosion film, which can act as possible sites for non-homogeneous nucleation [14, 53]. The positive effect of solution treatment on improving the corrosion resistance of the as-cast Mg–Cu, Mg–Sr, and Mg–Zn–Nd–Zr alloys has been reported previously [46, 52, 59].

Our results showed that the MDF-processed sample possessed the best corrosion resistance among the studied states (AC, ST, and MDF). Similar to the ST sample, the MDF processed sample shows a uniform microstructure, with few precipitates observed in the microstructure compared to the AC alloy. In addition, the grain size of the MDF sample is about 3.2 times smaller than the ST sample. This difference can significantly influence the corrosion resistance of Mg alloys in different ways, which are discussed and summarized below, but briefly, grain size affects the stability of the surface film.

It is well known that the precipitation process of the corrosion film begins on high-energy sites in the microstructure, such as grain boundaries. In addition, grain boundaries are known as high diffusivity paths for the diffusion of electrons and ions through the material. Accordingly, grain refinement increases the density of surface film nucleation and growth sites. Thus, the film formed on a fine-grained material is more homogeneous, with fewer cavities and defects. Such films would show high stability and provide better protection against corrosion compared to films formed on coarse-grained materials [44].

Grain boundaries are generally considered as defective crystalline regions with broken bonds, too many porosities, and dislocations that can reduce the tensile and compressive stresses in the surface film and thus, reduce the

probability of film cracking [41, 44]. Grain boundaries compensate for the mismatch between the matrix and the corroded layer [57]. Because the diffusion of reactants controls the corrosion kinetics, this uniform, crack-free, compact, and homogeneous film on fine-grained materials with good coherence [57] will create a cohesive barrier against diffusion [44], and thus, ceasing the corrosion process.

At last, it can be concluded that corrosion resistance of Mg alloys depends considerably on the quality of the surface film, where some secondary processes, such as heat treatment and severe plastic deformation, can significantly improve the quality of this film.

Step 3 According to the FESEM images of the corroded samples, and also the corrosion tests, it is obvious that the surface film of the AC, ST, and MDF specimens breaks after a specific immersion time. However, the intensity of film cracking is different in these samples. The AC specimen showed large cracks on the surface film, while the MDF specimen had the slightest cracks. The reasons for this behavior were discussed in previous sections.

The stresses present in the surface film may cause cracking of the surface film. This phenomenon is reflected in the Pilling–Bedworth ratio (PBR) value which is the ratio of compound (V_{com}) to metal (V_M) molar volumes and shows the stress conditions of the surface film formed on the alloy [41].

$$PBR = \frac{V_{com}}{V_M} = \frac{M_{com} \times \rho_M}{N \times A \times \rho_{com}} \tag{6}$$

where M_{com} is the molar weight of the compound, A is the atomic weight of the metal, ρ_{com} and ρ_M are the compound and metal densities, respectively, and n is the number of metal atoms in the compound molecule. If this ratio is less than one or greater than 2, the formed film does not have sufficient protection [41]. The tremendous deviation in the PBR values from one corresponds to the more significant stress in the surface film, and thus, more probability of crack formation. The PBR value for magnesium hydroxide, magnesium phosphate, and zinc phosphate are 1.8, 2.89, and 2.33, respectively. Therefore, the surface film composed of phosphate compounds has more significant stresses than the hydroxide film. Thus, the observed cracks on the surface films in region 3 of the hydrogen evolution curves can be related to these high stresses in the outer layer, which contained more phosphate compounds than the inner layer. Accordingly, it can be concluded that this increase in degradation rate in region III of the hydrogen evolution curves is mainly attributed to the film cracking, which exposes the underlying matrix to PBS, an effect that other researchers have reported [38, 41]. The amount and severity of film cracking depend on the compounds which exist in the film.

3.4 Cell Results

Figure 10a–d shows the SEM micrographs of L929 cells cultured on pure Mg, as the reference material, and the Mg–2Zn–0.2Ag alloy after 48 h of incubation. Also, Fig. 10e demonstrates the cell viability results for different samples tested for 24, 48 and 72 h. As it is evident in the SEM images, more cells, indicated by arrows, are attached to the alloy. Besides, the cell viability results demonstrate a two-fold increase in cell density in the alloy compared to pure Mg. This may be due to the positive effect of zinc element on the biocompatibility of Mg, which has previously been proven. In an investigation [60], adding 1% Zn to Mg–2Sr was shown to improve the viability of MG63 cell. In addition, surface morphology of pure Mg and the alloy in the culture environment may be another reason for the observed differences in cell response following exposure to each tested sample. According to Fig. 10, it is clear that the surface of pure Mg is smoother than the surface of the alloy.

It should be noted here that the DMEM culture medium contains chlorine ions [61], which dissolve the magnesium hydroxide layer, and thus, the new fresh Mg surface comes into contact with the culture medium again [62]. Due to the increase in surface passivity of the Mg–2Zn–0.2Ag alloy as the result of alloying with zinc [27], the dissolution process occurs much slower in these alloys compared with pure Mg. Therefore, the surface of the Mg–2Zn–0.2Ag alloy would be rougher than that of the pure magnesium, due to the more remained magnesium hydroxide on the surface of the alloy.

The fibrous morphology of the alloy surface (Fig. 10c and d) has caused more interaction of the cells with the alloy, and this factor has contributed to the cell growth and adhesion. In another research [63], the rougher surface of an Mg–6Zn alloy has caused enhanced cell attachment. Therefore, it is clear that the Mg–2Zn–0.2Ag alloy studied in this research shows an improved biological response compared to pure Mg and can, hence, be a suitable candidate for further research in implant fabrication studies.

4 Conclusions

The effect of solid solution treatment and MDF processing on the microstructure, mechanical, and corrosion properties of an Mg–2Zn–0.2Ag alloy was investigated. In addition, the biocompatibility behavior of the alloy was evaluated and compared with pure Mg. The main conclusions are summarized as follows.

(1) The MDF-processed and AC conditions showed the highest and lowest corrosion resistance. In fact, the surface film of the MDF-processed and ST specimens was more stable than the AC sample. Furthermore, unlike

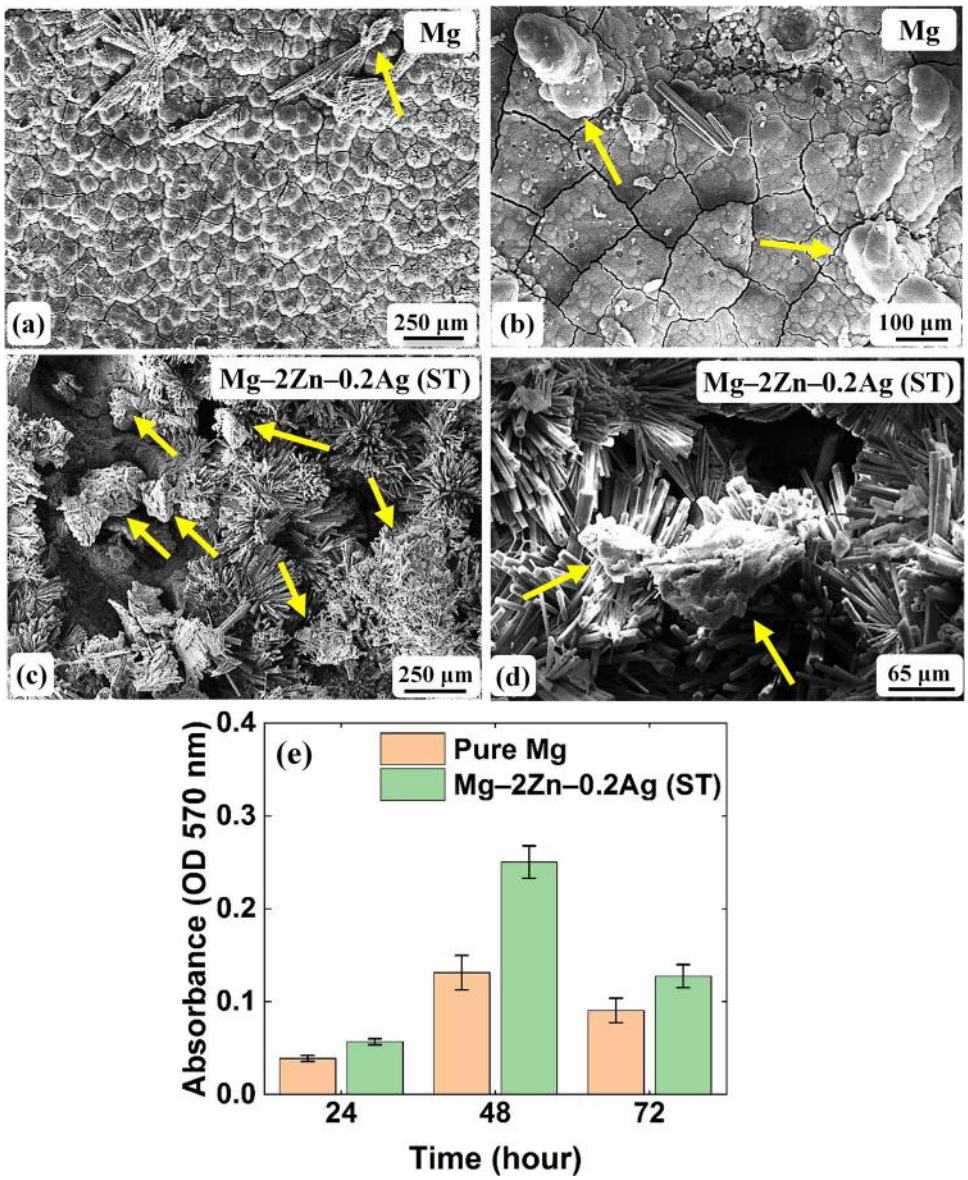

Fig. 10 SEM images showing cell adhesion on pure Mg (**a**, **b**) and solution-treated Mg–2Zn–0.2Ag alloy (**c**, **d**). Cell viability results are also given in (**e**)

the AC specimen, the MDF-processed and ST specimens did not suffer from micro galvanic corrosion.

(2) Two distinct layers were formed on the corroded surfaces. The inner layer was mainly magnesium hydroxide, while the phosphate compounds were found on the outer layer. The outer layer was susceptible to cracking, and the most cracking tendency was observed in the AC material.

(3) According to the cell studies, the cell adhesion and viability of the Mg–2Zn–0.2Ag alloy was found to be better than that of the pure magnesium.

(4) While solution treatment did not significantly change the mechanical properties of the Mg–2Zn–0.2Ag alloy, SYS, and USS of the MDF-processed alloy increased respectively by 16% and 25% compared to AC alloy.

Data availability The raw/processed data required to reproduce these findings cannot be shared at this time due to technical or time limitations.

Declarations

Conflict of interest The authors declare that they have no known competing financial interests or personal relationships that could have appeared to influence the work reported in this paper. The authors declare the following financial interests/personal relationships which may be considered as potential competing interests.

References

1. N. Hassanzadeh, T.G. Langdon, J. Mater. Sci.ci. **58**, 13721 (2023). https://doi.org/10.1007/s10853-023-08828-2
2. Y. Luo, C. Zhang, J. Wang, F. Liu, K.W. Chau, L. Qin, J. Wang, Bioact. Mater. **6**, 3231 (2021). https://doi.org/10.1016/j.bioactmat.2021.02.032
3. J. Wang, Y. Wu, H. Li, Y. Liu, X. Bai, W. Chau, Y. Zheng, L. Qin, Biomaterials **157**, 86 (2018). https://doi.org/10.1016/j.biomaterials.2017.12.007
4. K. Bryła, J. Horky, M. Krystian, L. Lityńska-Dobrzyńska, B. Mingler, Mater. Sci. Eng. C **109**, 110543 (2020). https://doi.org/10.1016/j.msec.2019.110543
5. U. Krishnaveni, S. Kumaran, Met. Mater. Int. **29**, 2093 (2023). https://doi.org/10.1007/s12540-022-01362-x
6. M. Johari, S.H. Tabaian, S. Saeedi, Met. Mater. Int. **28**, 1386 (2022). https://doi.org/10.1007/s12540-021-01010-w
7. J. Song, J. She, D. Chen, F. Pan, J. Magnes. Alloy. **8**, 1 (2020). https://doi.org/10.1016/j.jma.2020.02.003
8. M. Jamalpour, R. Alizadeh, Intermetallics **165**, 108133 (2024). https://doi.org/10.1016/j.intermet.2023.108133
9. M. Jamalpour, R. Alizadeh, Mater. Sci. Eng. A **859**, 144209 (2022). https://doi.org/10.1016/j.msea.2022.144209
10. M. Asadollahi, R. Alizadeh, S.K. Sadrnezhaad, J. Mater. Res. Technol. **26**, 1553 (2023). https://doi.org/10.1016/j.jmrt.2023.07.258
11. A. Nayeb-Hashemi, J.B. Clark, *Phase Diagrams of Binary Magnesium Alloys* (ASM International, Metals Park, 1988)
12. S. Ramesh, G. Anne, H.S. Nayaka, S. Sahu, M.R. Ramesh, J. Mater. Eng. Perform. **28**, 2053 (2019). https://doi.org/10.1007/s11665-019-04007-0
13. P. Metalnikov, G. Ben-Hamu, K.S. Shin, Met. Mater. Int. **27**, 1493 (2021). https://doi.org/10.1007/s12540-019-00529-3
14. Y. Song, E.-H. Han, D. Shan, C.D. Yim, B.S. You, Corros. Sci. **65**, 322 (2012). https://doi.org/10.1016/j.corsci.2012.08.037
15. H. Zhao, L.-Q. Wang, Y.-P. Ren, B. Yang, S. Li, G.-W. Qin, Acta Metall. Sin. English Lett. **31**, 575 (2018). https://doi.org/10.1007/s40195-018-0712-x
16. M.M. Zerankeshi, R. Alizadeh, E. Gerashi, M. Asadollahi, T.G. Langdon, J. Magnes. Alloy. **10**, 1737 (2022). https://doi.org/10.1016/j.jma.2022.04.010
17. Y. Lu, Y. Huang, F. Feyerabend, R. Willumeit-Römer, K.U. Kainer, N. Hort, Magnes. Technol. (2016). https://doi.org/10.1002/9781119274803.ch67
18. K. Bryła, J. Horky, Mater. Trans. **64**, 1709 (2023). https://doi.org/10.2320/matertrans.MT-MF2022056
19. E. Gerashi, R. Alizadeh, T.G. Langdon, J. Magnes. Alloy. **10**, 313 (2021). https://doi.org/10.1016/j.jma.2021.09.009
20. H. Yan, X. Gong, J. Chen, M. Cheng, Met. Mater. Int. **27**, 2249 (2021). https://doi.org/10.1007/s12540-019-00601-y
21. E. Koç, M.B. Kannan, M. Ünal, E. Candan, J. Alloys Compd. **648**, 291 (2015). https://doi.org/10.1016/j.jallcom.2015.06.227
22. E. Gerashi, R. Alizadeh, R. Mahmudi, J. Mater. Res. Technol. **20**, 3363 (2022). https://doi.org/10.1016/J.JMRT.2022.08.072
23. Y.F. Zheng, X.N. Gu, F. Witte, Mater. Sci. Eng. R Reports. **77**, 1 (2014). https://doi.org/10.1016/j.mser.2014.01.001
24. F. Witte, J. Fischer, J. Nellesen, H.-A. Crostack, V. Kaese, A. Pisch, F. Beckmann, H. Windhagen, Biomaterials **27**, 1013 (2006). https://doi.org/10.1016/j.biomaterials.2005.07.037
25. Z. Liu, R. Schade, B. Luthringer, N. Hort, H. Rothe, S. Müller, K. Liefeith, R. Willumeit-Römer, F. Feyerabend, Oxid. Med. Cell. Longev. (2017). https://doi.org/10.1155/2017/8091265
26. D. Tie, F. Feyerabend, W.-D. Mueller, R. Schade, K. Liefeith, K.U. Kainer, R. Willumeit, Eur. Cell. Mater. **25**, 284 (2013). https://doi.org/10.22203/ecm.v025a20
27. M. Asadollahi, E. Gerashi, R. Alizadeh, R. Mahmudi, J. Mater. Res. Technol. **21**, 4473 (2022). https://doi.org/10.1016/j.jmrt.2022.11.041
28. A. Dodangeh, M. Kazeminezhad, H. Aashuri, Mater. Sci. Eng. A **558**, 371 (2012). https://doi.org/10.1016/j.msea.2012.08.014
29. M. Atari, S. Labbaf, S. Haghjooy Javanmard, J. Polym. Environ. (2023). https://doi.org/10.1007/s10924-023-02957-0
30. Y. Jin, C. Blawert, H. Yang, B. Wiese, F. Feyerabend, J. Bohlen, D. Mei, M. Deng, M.S. Campos, N. Scharnagl, others. Mater. Des. **195**, 108980 (2020). https://doi.org/10.1016/j.matdes.2020.108980
31. S.W. Nam, W.T. Kim, D.H. Kim, T.S. Kim, Met. Mater. Int. **19**, 205 (2013). https://doi.org/10.1007/s12540-013-2010-5
32. D.-B. Liu, B. Wu, X. Wang, M.-F. Chen, Rare Met. **34**, 553 (2015). https://doi.org/10.1007/s12598-013-0052-y
33. E. Gerashi, M. Asadollahi, R. Alizadeh, R. Mahmudi, Mater. Sci. Eng. A **843**, 143127 (2022). https://doi.org/10.1016/j.msea.2022.143127
34. M. Sabbaghian, R. Mahmudi, K.S. Shin, J. Magnes. Alloy. **7**, 707 (2019). https://doi.org/10.1016/j.jma.2019.11.001
35. K. Yan, H. Liu, N. Feng, J. Bai, H. Cheng, J. Liu, F. Huang, J. Magnes. Alloy. **7**, 305 (2019). https://doi.org/10.1016/j.jma.2019.02.006
36. R. Alizadeh, J. LLorca, Acta Mater. **186**, 475 (2020). https://doi.org/10.1016/j.actamat.2020.01.028
37. K.B. Nie, X.J. Wang, K.K. Deng, F.J. Xu, K. Wu, M.Y. Zheng, J. Alloys Compd. **617**, 979 (2014). https://doi.org/10.1016/j.jallcom.2014.08.148
38. M. Ascencio, M. Pekguleryuz, S. Omanovic, Corros. Sci. **87**, 489 (2014). https://doi.org/10.1016/j.corsci.2014.07.015
39. S. Cai, T. Lei, N. Li, F. Feng, Mater. Sci. Eng. C **32**, 2570 (2012). https://doi.org/10.1016/j.msec.2012.07.042
40. M. Sabbaghian, R. Mahmudi, K.S. Shin, Mater. Sci. Eng. A **792**, 139828 (2020). https://doi.org/10.1016/j.msea.2020.139828
41. R.-C. Zeng, L. Sun, Y.-F. Zheng, H.-Z. Cui, E.-H. Han, Corros. Sci. **79**, 69 (2014). https://doi.org/10.1016/j.corsci.2013.10.028
42. S. Bender, J. Goellner, A. Heyn, S. Schmigalla, Mater. Corros. **63**, 707 (2012). https://doi.org/10.1002/maco.201106225
43. G. Song, A. Atrens, D. StJohn, Essent. Readings Magnes. Technol. (2016). https://doi.org/10.1007/978-3-319-48099-2_90
44. Y. Liu, D. Liu, C. You, M. Chen, Front. Mater. Sci. **9**, 247 (2015). https://doi.org/10.1007/s11706-015-0299-3
45. M. Sun, G. Wu, W. Wang, W. Ding, Mater. Sci. Eng. A **523**, 145 (2009). https://doi.org/10.1016/j.msea.2009.06.002
46. J. Chen, S. Wei, L. Tan, K. Yang, Mater. Technol. **34**, 592 (2019). https://doi.org/10.1080/10667857.2019.1603657
47. E. Gerashi, M. Jamalpour, R. Alizadeh, S. Labbaf, R. Mahmudi, Mater. Lett. **330**, 133224 (2023). https://doi.org/10.1016/j.matlet.2022.133224
48. F. El-Taib Heakal, A. Mohammed Fekry, M. Ziad Fatayerji, J. Appl. Electrochem. **39**, 583 (2009). https://doi.org/10.1007/s10800-008-9696-y
49. Y. Xin, K. Huo, H. Tao, G. Tang, P.K. Chu, Acta Biomater. **4**, 2008 (2008). https://doi.org/10.1016/j.actbio.2008.05.014
50. F.E.-T. Heakal, A.M. Fekry, M.Z. Fatayerji, J. Appl. Electrochem. **39**, 583 (2009). https://doi.org/10.1007/s10800-008-9696-y
51. A.F. Lotfabadi, H.R. Bakhsheshi-Rad, M.H. Idris, E. Hamzah, M. Kasiri-Asgarani, Can. Metall. Q. **55**, 53 (2016). https://doi.org/10.1179/1879139515Y.0000000031
52. X. Yan, P. Wan, L. Tan, M. Zhao, C. Shuai, K. Yang, Mater. Sci. Eng. B **229**, 105 (2018). https://doi.org/10.1016/j.mseb.2017.12.033
53. Y. Jang, B. Collins, J. Sankar, Y. Yun, Acta Biomater. **9**, 8761 (2013). https://doi.org/10.1016/j.actbio.2013.03.026
54. K.V. Kutniy, I.I. Papirov, M.A. Tikhonovsky, A.I. Pikalov, S.V. Sivtzov, L.A. Pirozhenko, V.S. Shokurov, V.A. Shkuropatenko,

Materwiss. Werksttech. **40**, 242 (2009). https://doi.org/10.1002/mawe.200900434
55. B.M. Wilke, L. Zhang, W. Li, C. Ning, C. Chen, Y. Gu, Appl. Surf. Sci. **363**, 328 (2016). https://doi.org/10.1016/j.apsusc.2015.12.026
56. R. Rettig, S. Virtanen, J. Biomed. Mater. Res. Part A An Off. J. Soc. Biomater. Japanese Soc. Biomater. Aust. Soc. Biomater. Korean Soc. Biomater. **88**, 359 (2009). https://doi.org/10.1002/jbm.a.31887
57. A. Bahmani, S. Arthanari, K.S. Shin, J. Magnes. Alloy. **8**, 134 (2020). https://doi.org/10.1016/j.jma.2019.12.001
58. Y. Song, E.-H. Han, D. Shan, C.D. Yim, B.S. You, Corros. Sci. **60**, 238 (2012). https://doi.org/10.1016/j.corsci.2012.03.030
59. J.-H. Dong, L.-L. Tan, Y.-B. Ren, K. Yang, Acta Metall. Sin. English Lett. **32**, 305 (2019). https://doi.org/10.1007/s40195-018-0750-4
60. K. Chen, X. Xie, H. Tang, H. Sun, L. Qin, Y. Zheng, X. Gu, Y. Fan, Bioact. Mater. **5**, 275 (2020). https://doi.org/10.1016/j.bioactmat.2020.02.014
61. M. Harjo, J. Torop, M. Järvekülg, T. Tamm, R. Kiefer, Polymers (Basel). **11**, 1043 (2019). https://doi.org/10.3390/polym11061043
62. M. Zohrevand, M. Mohammadi-Zerankeshi, F. Nobakht-Farin, R. Alizadeh, R. Mahmudi, J. Mater. Res. Technol. **20**, 1204 (2022). https://doi.org/10.1016/J.JMRT.2022.07.072
63. S. Zhang, J. Li, Y. Song, C. Zhao, X. Zhang, C. Xie, Y. Zhang, H. Tao, Y. He, Y. Jiang, Mater. Sci. Eng. C **29**, 1907 (2009). https://doi.org/10.1016/j.msec.2009.03.001

Publisher's Note Springer Nature remains neutral with regard to jurisdictional claims in published maps and institutional affiliations.

Springer Nature or its licensor (e.g. a society or other partner) holds exclusive rights to this article under a publishing agreement with the author(s) or other rightsholder(s); author self-archiving of the accepted manuscript version of this article is solely governed by the terms of such publishing agreement and applicable law.